

M DWARFS FROM HUBBLE SPACE TELESCOPE STAR COUNTS. IV.¹Zheng Zheng², Chris Flynn³, Andrew Gould^{2,4}, John N. Bahcall⁵, Samir Salim²

ABSTRACT

We study a sample of about 1400 disk M dwarfs that are found in 148 fields observed with the Wide Field Camera 2 (WFC2) on the Hubble Space Telescope and 162 fields observed with pre-repair Planetary Camera 1 (PC1), of which 95 of the WFC2 fields are newly analyzed. The method of maximum likelihood is applied to derive the luminosity function and the Galactic disk parameters. At first, we use a local color-magnitude relation and a locally determined mass-luminosity relation in our analysis. The results are consistent with those of previous work but with considerably reduced statistical errors. These small statistical errors motivate us to investigate the systematic uncertainties. Considering the metallicity gradient above the Galactic plane, we introduce a modified color-magnitude relation that is a function of Galactic height. The resultant M dwarf luminosity function has a shape similar to that derived using the local color-magnitude relation but with a higher peak value. The peak occurs at $M_V = 12$ and the luminosity function drops sharply toward $M_V = 14$. We then apply a height-dependent mass-luminosity function interpolated from theoretical models with different metallicities to calculate the mass function. Unlike the mass function obtained using local relations, which has a power-law index $\alpha = 0.47$, the one derived from the height-dependent relations tends to be flat ($\alpha = 0.10$). The resultant local surface density of disk M dwarfs ($12.2 \pm 1.6 \text{ M pc}^{-2}$) is somewhat smaller than the one obtained using local relations ($14.3 \pm 1.3 \text{ M pc}^{-2}$). Our measurement favors a short disk scale length, $H = 2.75 \pm 0.16$ (statistical) ± 0.25 (systematic) kpc.

Subject headings: stars: late-type { stars: low-mass, brown dwarfs { stars: luminosity function, mass function { stars: statistics { surveys

1. INTRODUCTION

M dwarfs dominate the luminous matter in the disk of the Galaxy. Thus it is important to study M dwarfs in order to constrain the disk mass and to understand the spatial distribution of stars in the disk. The mass function of M dwarfs may also give us some hints about the number of brown dwarfs whose masses are below the hydrogen-burning limit. Moreover, M dwarfs contribute to the observed microlensing events.

¹Based on observations with the NASA/ESA Hubble Space Telescope, obtained at the Space Telescope Science Institute, which is operated by the Association of Universities for Research in Astronomy, Inc. under NASA contract No. NAS5-26555.

²Department of Astronomy, Ohio State University, Columbus, OH 43210; zhengz@astronomy.ohio-state.edu, gould@astronomy.ohio-state.edu, samir@astronomy.ohio-state.edu

³Tuorla Observatory, Turku University, Väisälantie 20, FIN-21500, Piikkiö, Finland; c.flynn@astro.utu.

⁴Laboratoire de Physique Corpusculaire et Cosmologie, Collège de France, 11 pl. Marcelin Berthelot, F-75231, Paris, France

⁵Institute for Advanced Study, Princeton, NJ 08540; jnb@ias.edu

Star counts provide a straightforward way to explore the above questions. Work on star counts has a long history and developments of new techniques in detection and data reduction have made it a powerful tool to study the structure of the Galaxy (see Bahcall 1986 for a review). During the last twenty years, a variety of efforts have been made to count M dwarfs with ground-based observations (e.g. Hawkins & Bessel 1988; Tinney, Reid, & Gould 1993; Kirkpatrick et al. 1994).

Ground-based photometric studies and parallax studies generally deal with relatively nearby stars. Hence, they are not sensitive to the overall distribution of the stars in the Galactic disk and are subject to Malmquist bias. Observations made by the Hubble Space Telescope (HST) permit the resolution of much more distant stars. Hence, the overall distribution of stars in the disk can be measured more accurately. At the same time, Malmquist bias can be greatly reduced since the survey reaches the "top" of the disk. The present study is the culmination of almost a decade of work on HST star counts, beginning with counts using the pre-repair Planetary Camera (PC1) (Gould, Bahcall, & Mazur 1993) and the first much deeper counts with the repaired Wide Field Camera (WFC2) (Bahcall et al. 1994). Gould, Bahcall, & Flynn (1996, hereafter Paper I) studied a sample of 257 Galactic disk M dwarfs which include 192 stars in 22 fields observed with WFC2 with mean limiting magnitude $I = 23.7$ and 65 stars in 162 fields observed with PC1 with mean limiting magnitude $V = 21.3$. In this paper, V and I denote magnitudes in Johnson-Cousins systems. They derived a disk luminosity function (LF) peaking at $M_V = 12$ and dropping off sharply between $M_V = 12$ and $M_V = 14$. The total column density of M dwarfs at the Galactocentric radius $R_0 = 8.0$ kpc was determined to be $12.4 \pm 1.9 \text{ M pc}^{-2}$. The scale length for the M-star disk was found to be 3.0 ± 0.4 kpc. In a follow-up paper, Gould, Bahcall, & Flynn (1997, hereafter Paper II) incorporated 80 additional M dwarfs found in 31 new fields observed with WFC2 into their data set. The overall results were consistent with Paper I but with somewhat smaller error bars.

In this paper, we analyze the disk M dwarfs found in an additional 95 WFC2 fields. After combining these 95 fields with the fields studied in Papers I and II, our sample of disk M dwarfs now includes about 1400 stars, almost three times larger than the sample studied in Paper II. The large sample helps to reduce the statistical uncertainties, especially at the faint end of the LF. Although the underlying method is the same as that used in Papers I and II, we make several modifications in this paper. First, we find that the errors of V and I magnitudes are slightly underestimated in previous work due to a bug in the computer code. We correct this bug. For most of the stars, the correction is negligibly small. However, this correction has a relatively larger effect for the last M_V bin. Second, in this paper, we adopt a slightly revised photometric transformation from WFC2 instrumental to standard Johnson-Cousins magnitudes, which is derived through an empirical calibration and is described in the Appendix. Third, we take the metallicity effect on the color-magnitude relation (CMR) into account. Based on the color-magnitude diagram by Reid (1991) and Monet et al. (1992), we add a term varying with the Galactic height z which is designed to model the metallicity effect. We then interpolate the mass- M_V relations based on different metallicities (Baran et al. 1998) to derive the mass function, rather than simply using the local (solar metallicity) relation of Henry & McCarthy (1993) as was done previously.

The main results of this paper are: First, if we use the original solar-neighborhood CMR (Reid 1991), the overall results are consistent with those in Paper I and II but with considerably smaller statistical errors. The M dwarf mass function has a power-law index $\alpha = 0.47$ in the range of 0.08 M_\odot to 0.5 M_\odot . Second, if we adopt the modified z -dependent CMR, the best fit scale heights and scale lengths in our models are about 20–30% smaller. The local M dwarf mass density and surface density are about 15% smaller than those using the solar-neighborhood CMR, and the mass function is roughly flat, $\alpha \approx 0.10$.

2. OBSERVATIONS AND DATA ANALYSIS

2.1. Observations

In this paper, we include three sets of data (data in Paper I, new data in Paper II, and new fields in this paper). Altogether we include 148 fields imaged with WFC2 and 162 fields imaged with PC1. The WFC2 fields were chosen to satisfy the following criteria: first, the Galactic latitude $|b| > 17^\circ$; second, there should be at least 2 exposures with the F814W filter and at least one with F606W filter for each field; third, in these fields, there should be no Local Group galaxies or globular clusters in our Galaxy or other galaxies. The 162 PC1 fields are taken from 166 QSO snapshot survey fields (Bahcall et al. 1992; Maoz et al. 1993) for which the QSOs were selected by radio, X-ray, and color-excess techniques. Four PC1 fields were excluded because ground-based observations could not be obtained.

We set two magnitude limits for each field observed with WFC2. The faint magnitude limit I_{max} denotes our detection threshold. This limit ensures that the discrimination between stars and galaxies is clear. The bright magnitude limit I_{min} represents the saturation threshold. Details on these two limits can be found in Paper I.

The photometry for the stars in the 162 fields imaged with PC1 is based on ground observations (see Paper I). These stars with non-HST photometry occupy an important part of parameter space. Generally speaking, the stars found in these fields would have been saturated in WFC2 data because they have relatively small Galactic heights and high luminosities. Hence, these stars (denoted by open circles) provide much of the data occupying the lower-left part of the $z - M_V$ plane shown in Figure 1.

The previous 53 WFC2 fields and 162 PC1 fields are described in Paper I and Paper II in detail. Table 1 lists the characteristics of the 95 newly incorporated WFC2 fields in order of ascending Galactic latitude, where I_{max} and I_{min} are the detection threshold and the saturation threshold in I band, respectively. The fraction of the 4.4 arcmin^2 effective area of the WFC2 covered by each field is denoted by f . The fields with $l = 180^\circ$ and $b = 22^\circ$ are near the Hyades cluster. However, by checking the color-magnitude diagram (CMD) of these fields, we conclude that they are not contaminated by cluster stars. The field near $l = 355^\circ$ and $b = 23^\circ$ has one 20 s exposure and two 200 s exposures with the F814W filter so that the stars selected from this field appear substantially brighter than most WFC2 field and so make a significant contribution to the lower-left part of the $z - M_V$ plane (Fig. 1).

In Paper I and Paper II, the transformation from HST instrumental magnitudes to the standard Johnson-Cousins system was based on a synthetic calibration by Bahcall et al. (1994). The red end of this calibration was based on M giants rather than M dwarfs due to availability. Strictly speaking, their transformation applies to observations made before the WFC2 CCD cooldown on 23 Apr. 1994. In this paper we adopt a modified form of the transformation based on an empirical calibration that uses M dwarfs rather than giants. This transformation can apply to observations made either before or after the cooldown by using different zero points. The difference between this calibration and the calibration by Bahcall et al. (1994) without chip-to-chip offsets is small. For example at $V - I = 3$, the differences are: 0.02 mag in V and 0.03 mag in I before the cooldown; and 0.06 mag in V and 0.04 mag in I after the cooldown. The difference between this calibration and that given by Holtzman et al. (1995) for the post-cooldown period is also very small: at $V - I = 3$, the differences in I and in V are about 0.02 mag and 0.05 mag, respectively. We describe the calibration in detail in the Appendix.

For each field, the extinction A_B is derived from Burstein & Heiles (1982). As in Paper I, we adopt $A_V = 0.75A_B$, $A_I = 0.57A_V$, $A_{V^0} = 0.91A_V$ (V^0 denotes F606W filter) and $A_{I^0} = 0.59A_V$ (I^0 denotes

Table 1. Characteristics of the 95 New WFC2 Fields

R A . (2000)	Dec. (2000)	l ()	b ()	I _{m ax}	I _{m in}	(WFC2)
11 41 53.35	80 31 55.6	299.97	18.06	23.29	18.64	1.00
21 51 08.26	+ 29 00 00.3	81.96	19.18	23.98	19.45	1.00
21 50 34.47	+ 28 50 37.9	81.75	19.22	24.43	19.76	1.00
21 51 21.87	+ 28 44 05.9	81.81	19.42	23.90	19.76	1.00
07 50 47.13	+ 14 40 44.2	206.07	19.63	23.42	19.45	1.00
04 32 07.19	+ 17 57 17.1	179.16	20.06	21.60	16.90	1.00
17 55 26.65	+ 18 18 17.8	43.68	20.34	24.21	19.45	1.00
04 21 37.47	+ 19 31 48.8	176.17	20.95	23.28	18.84	1.00
04 25 17.16	+ 17 42 57.4	178.26	21.47	22.81	17.65	1.00
06 15 45.38	+ 70 57 40.8	143.38	22.71	22.42	17.65	1.00
16 11 33.45	18 38 27.6	355.19	23.33	21.66	14.40	1.00
04 09 41.07	+ 17 04 19.5	176.15	24.71	23.47	18.84	1.00
09 09 57.87	09 27 42.9	239.28	25.08	24.00	19.76	1.00
13 22 12.29	36 41 22.6	309.78	25.77	23.53	17.89	1.00
06 11 18.08	48 47 56.4	256.51	26.44	24.51	19.87	1.00
19 38 10.83	46 19 50.2	352.31	27.02	24.09	19.84	1.00
17 36 39.19	+ 28 04 11.2	52.06	27.79	23.30	16.51	1.00
17 36 23.05	+ 28 01 01.1	51.98	27.83	23.29	18.64	1.00
07 39 14.98	+ 70 22 58.3	145.09	29.43	23.36	18.75	1.00
19 40 41.24	69 15 56.3	326.37	29.58	24.16	19.45	1.00
19 41 03.27	69 11 52.4	326.45	29.61	22.96	18.09	1.00
13 39 41.64	31 34 14.5	314.82	30.18	23.41	18.64	1.00
16 30 36.09	+ 82 29 35.1	115.76	31.27	23.89	18.53	1.00
08 11 58.81	+ 75 00 30.6	139.45	31.31	23.52	18.64	1.00
03 55 31.55	+ 09 43 33.5	179.83	32.15	23.52	18.26	1.00
11 21 28.23	24 55 15.8	278.31	33.61	23.28	18.64	1.00
12 53 01.47	29 14 15.5	303.35	33.63	24.32	19.45	1.00
17 12 23.18	+ 33 35 41.6	56.72	34.25	24.25	19.45	1.00
08 30 43.55	+ 65 50 27.9	149.78	34.68	23.88	19.15	1.00
04 55 54.74	21 55 09.5	221.88	34.68	22.81	18.09	1.00
08 31 03.47	+ 65 50 06.7	149.78	34.71	24.01	19.50	1.00
03 05 16.46	+ 17 28 18.5	162.78	34.84	23.35	18.75	1.00
03 05 30.00	+ 17 09 56.5	163.06	35.06	23.32	18.75	1.00
08 54 16.58	+ 20 03 37.6	206.82	35.69	23.83	19.45	1.00
20 44 45.80	31 19 19.4	12.65	36.72	22.40	17.65	1.00
10 05 46.00	07 41 24.5	247.87	36.90	24.28	19.45	1.00
16 57 51.54	+ 35 25 42.3	58.26	37.53	24.04	18.64	1.00
14 41 53.03	17 18 38.0	337.15	38.11	24.13	19.73	1.00
02 38 19.44	+ 16 39 13.7	156.66	39.12	23.06	18.64	1.00
16 01 12.86	+ 05 36 02.5	16.22	40.06	24.09	18.64	1.00
21 57 11.22	69 49 29.1	321.17	40.57	24.27	18.75	1.00
16 09 12.21	+ 65 32 00.0	98.33	40.90	24.06	19.80	1.00
16 42 18.38	+ 39 46 14.8	63.39	41.08	24.51	19.55	1.00
04 07 31.31	12 08 33.2	204.82	41.80	22.53	17.65	1.00
14 49 56.96	10 06 03.5	344.63	42.97	23.92	19.76	1.00
16 24 12.97	+ 48 09 08.8	74.92	44.06	23.46	18.75	1.00
01 15 51.87	+ 16 41 57.3	131.33	45.77	22.39	17.89	1.00
00 17 11.03	+ 15 48 54.5	110.97	46.26	23.13	18.93	1.00

Table 1. Characteristics of the 95 New WFC2 Fields | Continued

R A . (2000)	Dec. (2000)	l ()	b ()	I _{m ax}	I _{m in}	(WFC2)
09 39 33.74	+ 41 32 46.1	179.88	48.45	23.91	19.22	1.00
10 56 59.04	03 35 27.8	256.54	48.69	23.25	18.64	1.00
15 43 24.56	+ 53 52 45.9	85.35	48.77	24.30	19.84	1.00
22 32 55.80	60 33 01.1	328.25	49.21	23.97	19.40	1.00
00 53 36.12	+ 12 49 46.1	123.75	50.04	23.87	19.45	1.00
00 53 23.16	+ 12 33 57.7	123.68	50.30	23.54	19.45	1.00
14 00 13.84	+ 62 33 42.4	109.91	52.79	23.71	18.84	1.00
13 59 59.37	+ 62 33 42.5	109.95	52.81	23.65	18.84	0.95
14 00 06.58	+ 62 31 06.5	109.90	52.84	23.67	18.84	0.95
13 59 52.14	+ 62 31 06.6	109.94	52.85	23.71	18.84	0.92
13 59 37.69	+ 62 31 06.5	109.98	52.86	23.71	18.84	0.93
14 00 13.77	+ 62 28 30.4	109.85	52.87	23.67	18.84	1.00
13 59 23.24	+ 62 31 06.4	110.03	52.87	23.67	18.84	0.94
13 59 59.35	+ 62 28 30.5	109.89	52.88	23.63	18.84	0.96
13 59 44.92	+ 62 28 30.5	109.93	52.90	23.62	18.84	0.96
13 59 30.50	+ 62 28 30.4	109.97	52.91	23.70	18.84	0.96
10 24 51.70	+ 47 05 33.1	168.18	55.10	23.18	18.64	1.00
15 19 54.79	+ 23 44 53.3	35.59	56.43	23.92	19.28	1.00
14 41 00.08	+ 53 26 59.2	92.90	56.81	23.34	18.64	1.00
01 24 41.93	+ 03 51 26.1	138.73	57.99	24.19	19.72	1.00
13 36 17.10	00 52 02.8	325.81	60.00	23.87	17.34	1.00
12 36 39.59	00 41 58.0	295.06	61.95	23.64	18.26	1.00
14 42 30.88	+ 35 24 22.1	59.12	64.96	22.84	18.09	1.00
00 50 31.47	52 09 55.0	303.26	64.96	22.80	17.18	1.00
00 50 32.91	52 07 18.5	303.26	65.01	23.33	18.64	0.97
00 50 12.11	52 03 51.7	303.38	65.06	23.69	19.08	1.00
12 34 08.55	+ 02 44 33.8	292.56	65.27	23.63	18.75	1.00
13 53 29.96	+ 48 32 55.8	97.73	65.43	24.14	19.76	1.00
11 46 02.35	+ 47 34 03.4	150.64	65.89	22.54	17.65	1.00
11 46 14.53	+ 47 33 53.6	150.58	65.91	22.83	18.09	1.00
12 17 54.57	+ 50 12 11.8	136.22	66.05	24.24	19.87	1.00
11 16 27.41	+ 18 05 42.7	230.38	66.35	23.91	19.28	1.00
14 35 33.34	+ 25 18 09.0	34.37	66.62	24.06	18.64	1.00
11 48 21.38	+ 10 50 03.1	257.58	67.96	23.16	18.09	1.00
14 04 28.90	+ 43 19 12.3	85.29	68.08	24.34	19.80	1.00
11 48 49.73	+ 10 55 05.9	257.68	68.10	23.94	18.26	1.00
11 48 50.97	+ 10 57 56.2	257.61	68.14	24.13	19.55	1.00
12 27 45.96	+ 44 07 58.1	137.05	72.34	22.96	18.26	1.00
12 10 33.65	+ 39 28 58.7	154.88	75.00	23.93	18.26	1.00
00 15 47.24	16 19 06.3	83.73	76.39	23.27	18.64	1.00
00 15 55.35	16 18 06.2	83.88	76.40	23.12	18.64	1.00
11 50 29.28	+ 28 48 33.4	202.26	76.45	24.11	19.45	1.00
13 16 28.86	+ 36 27 16.1	94.83	79.27	22.81	18.09	1.00
13 24 49.72	+ 30 58 36.0	62.72	81.75	24.87	19.55	1.00
12 47 47.30	+ 34 32 57.3	128.73	82.54	23.25	18.64	1.00
00 24 54.07	27 16 17.7	30.02	84.10	24.14	19.76	1.00
13 00 23.85	+ 28 20 06.1	64.77	87.68	23.31	18.64	1.00

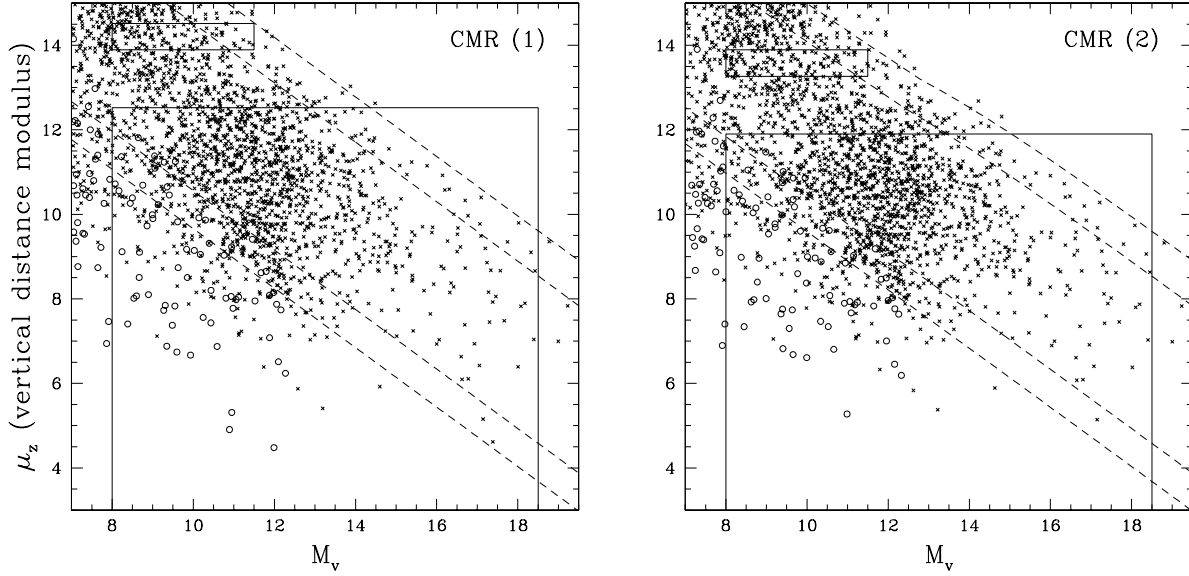


Fig. 1. Stars in all the fields shown in the $\mu_z - M_V$ plane, where $\mu_z = 5 \lg z - 5 = V_0 - M_V + 5 \lg \sin \beta$ is the Galactic height modulus and M_V is the absolute V magnitude inferred from the color. The left and right panels are derived using the solar-neighborhood CMR (1) and the z -dependent CMR (2), respectively. Crosses and circles represent stars from the 148 WFC2 fields and 162 PC1 fields, respectively. Diagonal lines denote the I-band range of sensitivity of the fields: half of the fields have limits $I_{\text{max}} + 5 \lg \sin \beta$ that lie between the two upper-right lines, while one quarter lie above the upper line of these two upper-right lines and one quarter below the lower line. Similarly for $I_{\text{min}} + 5 \lg \sin \beta$ and the two lower-left lines. Stars satisfying our selection criteria (see text) fall into the large box. The small box is believed to contain only spheroidal subdwarfs.

F814W filter) to deredden all the stars.

2.2. Sample Selection

To derive the absolute magnitude, as in Paper I and Paper II, at first we adopt the solar-neighborhood CMR determined by Reid (1991):

$$M_V = 2.89 + 3.37(V - I) \quad (1)$$

with a dispersion of 0.44 mag.

The large sample substantially reduces the statistical errors relative to those reported in Paper II. In particular, the error in the disk scale length is reduced dramatically. Hence, systematic errors become more significant. We therefore explore the effect of metallicity variations on our result. As the Galactic height increases, more and more disk dwarfs with lower metallicity will be detected, and these tend to be less luminous than the dwarf stars near the Galactic plane at the same $V - I$ color. Hence we modify the above CMR by adding a term that varies with the Galactic height z :

$$M_V = 2.89 + 3.37(V - I) + f(z)m(V - I); \quad (2)$$

where

$$f(z) = \begin{cases} \frac{z_j}{1.5 \text{ kpc}}; & |z_j| \leq 1.5 \text{ kpc} \\ 1; & |z_j| > 1.5 \text{ kpc} \end{cases}$$

and

$$m(V-I) = \begin{cases} 0.2(V-I); & (V-I) \leq 2.5 \\ 1 - 0.2(V-I); & (V-I) > 2.5 \end{cases} \quad (3)$$

Figure 1 in Reid (1991) and Figure 10 in Monet et al. (1992) show a color-dependent dispersion in the color-magnitude relation: the dispersion is peaked at $(V-I) \approx 2.5$ and becomes smaller towards redder and bluer colors. We estimate this dispersion to be $m(V-I)$ as given in equation (3). We then also adopt this $m(V-I)$ as the scale of the offset in M_V as a function of height (eq. [2]). That is, we assume that the observed scatter is due to metallicity variation and hence assume that the amplitude of the metallicity effect with height is proportional to this scatter. It should be pointed out that this ad hoc CMR does not necessarily represent the true metallicity effect on main sequence stars at different Galactic height. However, this CMR is adequate for our purposes: making a first-order correction for the metallicity effect and estimating the systematic errors due to this correction.

Stars in our sample are chosen to satisfy both a luminosity criterion and a Galactic height criterion: $8.0 < M_V < 18.5$. This corresponds to $1.53 < V-I < 4.63$ under the CMR (1). The blue boundary prevents contamination by spheroidal giants (Green, Demarque, & King 1987), and the red boundary is about the red edge of the color-magnitude diagram of Monet et al. (1992) (although the CMR becomes double-valued at $V-I \approx 4.4$ in this diagram, the relatively small number of dwarfs fainter than $M_V = 18.5$ makes this effect negligible in our analysis); Galactic height z must be below 3200 pc if the solar-neighborhood CMR (1) is used and below 2400 pc if the z -dependent CMR (2) is used in order to avoid the contamination by spheroidal dwarfs (see Paper I & Paper II).

When CMR (1) is adopted, altogether, in the 148 WFC fields and 162 PC1 fields, 1413 stars satisfy our selection criteria: 263 in the fields analyzed in Paper I, 85 in the 31 additional fields analyzed in Paper II, and 1065 in the 95 new fields. Note that the numbers of stars in the previous fields differ slightly from those in Paper I and Paper II because of a slight change in the transformations from WFC2 instrumental magnitudes to standard Johnson-Cousins magnitudes as mentioned in §2.1. If we use the modified CMR (2), the total number of selected stars is 1373.

The distribution of stars in the sample as a function of R , the cylindrical distance from the Galactic center and as a function of height, z , above the plane is shown in Figure 2 for the cases based on the solar-neighborhood CMR (1) and the z -dependent CMR (2). The mean and standard deviation of Galactocentric radius of all stars is $\bar{R} = 7.7 \pm 1.7$ kpc for CMR (1) and $\bar{R} = 7.7 \pm 1.4$ kpc for CMR (2). The lower panels of Figure 2 show the histogram of the heights above the Galactic plane for each case. We plot the fraction of stars weighted by $(R - \bar{R})^2$ as well as the nonweighted one. The weight factor comes from equation (2.1) and (2.3) of Gould (1995) with $f(R; H) = \exp(-R/H)$. The weighted plot tells us the stars at which height dominate our derivation of the slope of the radial distribution of disk stars and thus of the scale length of the disk. There is almost no weight from stars with height $z < 1$ kpc. The average weighted height \bar{z} is about 2 kpc for CMR (1) and is about 1.5 kpc for CMR (2). As we discuss in §3, this implies that our final results on the disk profiles are primarily based on stars well above the thin disk population.

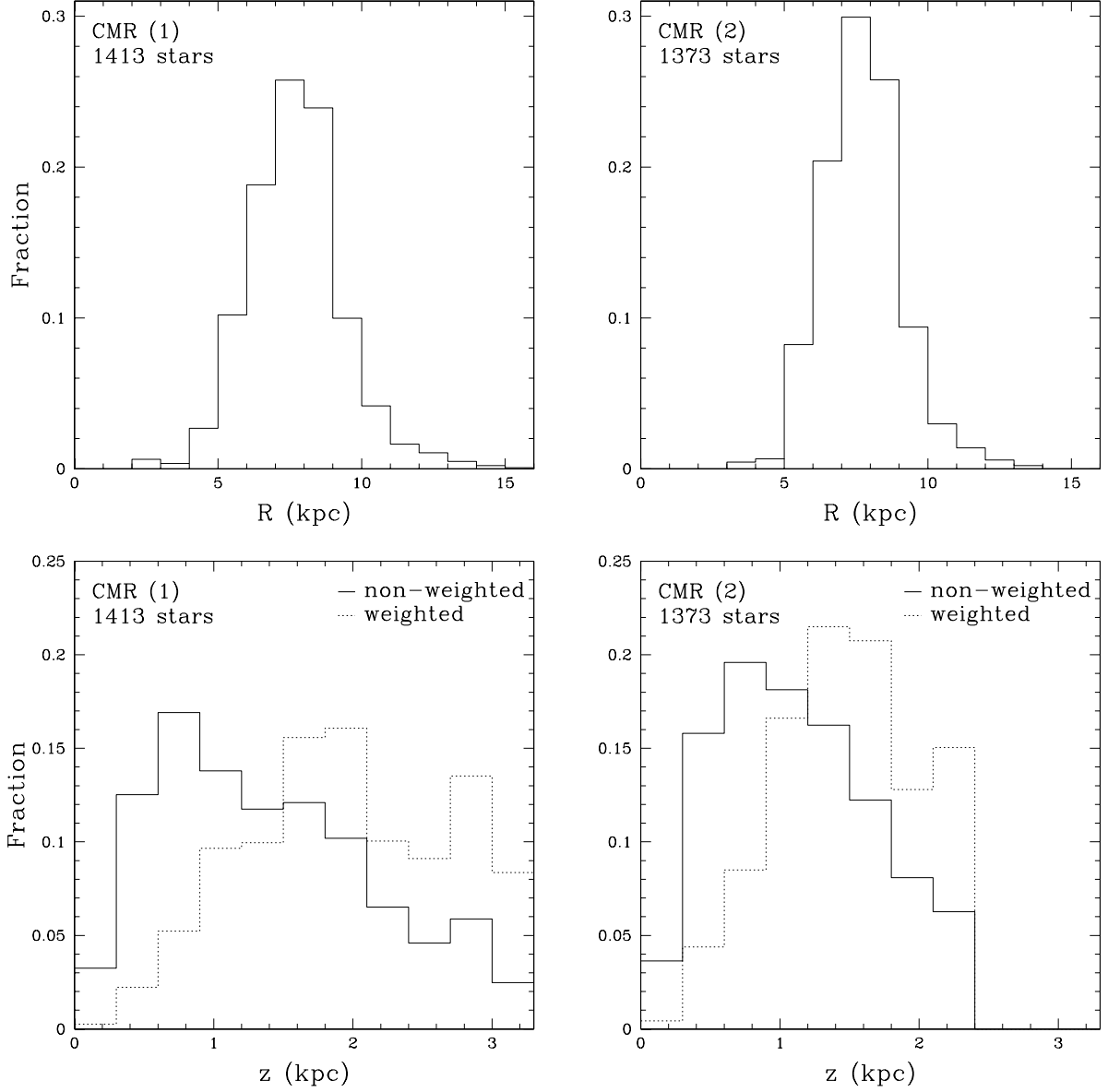


Fig. 2. The distribution of stars in our sample as a function of the Galactic coordinates (R, z) . CMR (1) and (2) are used in the left and right histograms, respectively. The Galactic height distribution weighted by $(R - \bar{R})^2$ is shown as dotted lines in the lower panels.

2.3. Models and Method

The luminosity function (LF) of disk M dwarfs is modeled as a function of Galactic position (R, z) by

$$(i; z; R) = \phi_i(z) \exp \left(-\frac{R - R_0}{H} \right); \quad (4)$$

where ϕ_i is the LF for the i th magnitude bin in the solar neighborhood, $R_0 = 8$ kpc is the Galactocentric distance of the Sun, and H is the scale length of the disk. The density profile $\phi_i(z)$ is assumed to have either a "sech²" form,

$$\phi_i(z) = (1 - \epsilon_i) \text{sech}^2 \frac{z}{h_1} + \epsilon_i \exp \left(-\frac{|z|}{h_2} \right) \quad (5)$$

or a "double exponential" form,

$$\phi_i(z) = (1 - \epsilon_i) \exp \left(-\frac{|z|}{h_1} \right) + \epsilon_i \exp \left(-\frac{|z|}{h_2} \right); \quad (6)$$

The method of maximum likelihood (see Paper I) is applied to derive simultaneously the LF ϕ_i at each magnitude bin and the disk profile parameters (h_1, h_2, ϵ_i) . The magnitude bins are centered at $M_V = 8.25, 9, 10, 11, 12, 13, 14, 15.5, 17.5$, respectively. The size of each bin is 1 mag except the first one (0.5 mag) and the last two (2 mag). Given a value of the disk scale length H , a solution of the above 12 parameters is found by maximum likelihood. Then, the scale length is determined by maximizing the likelihood over the ensemble of solutions using different values of H .

3. RESULTS

The derived parameters fall into two categories: the LF ϕ_i at each magnitude bin and the disk profile parameters such as the scale length. As discussed in Paper I and Paper II, there are almost no stars near the Galactic plane in our sample so that we lack information on the local stellar density. Hence, there is a degeneracy between the best fits of the sech² model and the double exponential model which cannot be resolved by our HST data alone. Therefore we must normalize the HST LF using LFs derived by other methods. We therefore discuss the LF first and then examine the disk parameters. Finally we convert the LF to a mass function.

3.1. Luminosity Function

The best fit LF for the sech² model and that for the double exponential model have nearly the same shape but differ from each other in normalization. For example, in the case of using the z -dependent CMR (2), the exponential model has a normalization 1.5 times that of the sech² model. This normalization difference is compensated by the vertical density profile: in the same example, the vertical density of the sech² model is almost 1.5 times larger than that of the exponential model everywhere except in the vicinity of the plane (where there are few data). We therefore perform a linear combination of the LFs in these two models. The combination coefficient is obtained by normalizing the combined LF using the local LF in the region $8.5 < M_V < 12.5$ derived by Wielen, Jahreiss, & Kruger (1983). It turns out that the sech² model agrees fairly well with the local-star normalization: for CMR (1), the relative difference from the local normalization is less than 0.3%; for CMR (2), the relative difference from the local normalization is less

than 10% . In the case of the double exponential model, the relative differences from the local normalization are much larger, 93% and 65% for CM R (1) and CM R (2), respectively. Note that the relative errors of the LF given by Wielen et al. (1983) increase from 10% to 30% in the above magnitude range.

We compare the LFs derived using different data sets in Figure 3. In Table 2, we also list LFs derived using all the available data and adopting different CM Rs. Assuming CM R (1), our new result is consistent with those derived in Paper I and Paper II. The statistical errors are reduced considerably. The last data point in this plot (centered at $M_V = 17.5$ with a bin width of 2 magnitudes) drops from $3.4 \times 10^3 \text{ pc}^3 \text{ mag}^{-1}$ to $2.5 \times 10^3 \text{ pc}^3 \text{ mag}^{-1}$. The main reason for this is our correction of the error estimation as well as a small contribution from the new transformations that we adopt. This last data point had caused a worry in Paper I and Paper II because it was much higher than the result from naive binning. The new result confirms that the maximum likelihood method yields a reasonable value for the last point. We note that the good agreement between the Paper II results based on naive binning and the corrected maximum-likelihood calculation shows that the effects of Malmquist bias are small. This is because naive binning ignores the dispersion in the CM R, and so ignores Malmquist bias, while maximum likelihood automatically compensates for Malmquist bias (assuming that the adopted dispersion in the CM R is correct). Ignoring the first half magnitude bin (for which boundary effects are important) the fractional difference in the two methods averages 10% . As we argued in Papers I and II, the small size of this effect is due to the fact that the sample extends to the "top" of the disk.

The LF peaks at about $M_V = 12$ and still shows a sharp drop towards $M_V = 14$, as mentioned in Paper I and Paper II. Reid & Gizis (1997) showed that there might be some fine structures in the CM R (see their Fig. 13). We attempted to use their new analytic fit of the CM R in our analysis. It leads to a much steeper slope of the LF in the range of 12 mag to 14 mag. The physical reason is that their fit has a relatively larger slope, 9.74 instead of 3.37, in this region. This larger slope makes the magnitude range $12 < M_V < 14$ correspond to a smaller color range (~ 0.2 mag) and hence fewer stars. However, it is possible that the "steep" part of the CM R discussed by Reid & Gizis (1997) may differ for lower-metallicity stars (most likely shifted blueward, see Fig. 7 of Gizis 1997). Such a blueward shift in the steep section of the CM R would help smooth the LF, and would be quite plausible because the majority of the HST sample is likely to be more metal-poor than the Reid & Gizis (1997) stars. However, there do not appear to be any available data sets at lower metallicity that would allow us to verify the reality of such a shift nor to measure its size. We therefore adopt the original Reid (1991) law (see eq. (1)). We note, however, that this means that we cannot be sure that the sharpness of the drop in the LF between $M_V = 12$ and $M_V = 14$ is real.

Adopting the z-dependent CM R (2) leads to the LF having a slight horizontal shift towards the faint end with respect to the above LF. This is not surprising since at the same color, stars tend to be fainter under this CM R. The LF still peaks at $M_V = 12$ with a higher peak value and becomes more symmetric about this peak. The biggest difference in LFs for cases of CM R (1) and CM R (2) occurs around the peak. This is the reflection of the fact that the z-dependent CM R (2) has, at a given Galactic height, the largest correction at $V - I = 2.5$ and smaller corrections toward redder and bluer colors.

The consistency of the results presented here with those derived in Paper I and Paper II (the latter based on only about 1/4 of the total sample) demonstrates the stability of our method and also of the underlying data set which has been assembled from Hubble Space Telescope observations over almost a decade. Because these data were taken by two different instruments (WFC2 and PC1), it is also important to compare the LF found using all the data with that derived using only WFC2 data. Since the PC1 data comprise only about 5% of the full sample, one might not expect their exclusion to have much impact.

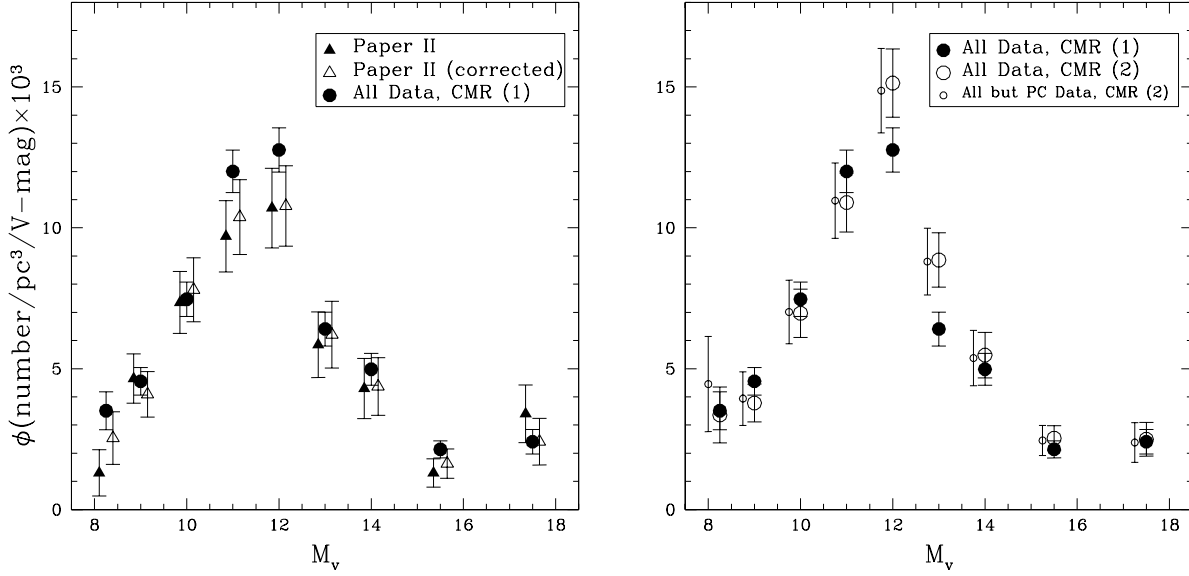


Fig. 3. Normalized luminosity functions derived using the method of maximum likelihood. The left panel shows the comparison of LFs determined using different data sets. Here the solar-neighborhood CMR (1) is adopted. The result of Paper II and that of Paper II with the correction of error estimation and magnitude transformation are displayed together with the LF determined by all the data available. These three LFs are slightly displaced along the horizontal direction with respect to each other in order to make the figure easier to read. The right panel shows the comparison between LFs determined using CMR (1) and the z -dependent CMR (2). For comparison, in the right panel we also plot the LF (slightly displaced along the horizontal direction) derived using only WFC2 data and CMR (2) (see the text for details).

Table 2. Normalized Luminosity Functions

(Both LFs are derived using all the available data.)

M_v (mag)	[CMR (1)] ($10^{-3} \text{ pc}^{-3} \text{ V-mag}^{-1}$)	[CMR (2)] ($10^{-3} \text{ pc}^{-3} \text{ V-mag}^{-1}$)
8.25	3.51 0.67	3.36 0.99
9.00	4.56 0.49	3.78 0.67
10.00	7.46 0.61	6.97 0.86
11.00	12.00 0.75	10.90 1.05
12.00	12.76 0.78	15.14 1.21
13.00	6.41 0.60	8.86 0.96
14.00	4.98 0.57	5.48 0.81
15.50	2.14 0.30	2.53 0.44
17.50	2.41 0.43	2.49 0.60

However, as was pointed out in the discussion of Figure 1, the PC1 data tend to dominate the sample for the bright end of the LF. We see from Figure 3 that indeed inclusion of these data reduces the error bars of the first few LF bins by 25{40%. Note that in the brightest bin where the PC1 data clearly dominate, the two LFs are consistent. We conclude that the underlying data set is self-consistent.

3.2. Disk Parameters

We summarize the best-fit disk parameters for M dwarfs in Table 3. The first two lines are the original results in Paper I and Paper II, respectively. The third line is the corrected result for Paper II: the error estimation mentioned in §1 is corrected and the new transformation formulae are applied. Next are the best fits using only WFC2 data with the solar-neighborhood CMR (1) and the z-dependent CMR (2) being adopted, respectively. Finally, we list the best fits using all the data available with CMR (1) and CMR (2), respectively. For the last four cases, we list the results of the sech^2 model, the double exponential model and the normalized model (see §3.1). To derive the local mass density ρ_0 and the column density Σ_M of M dwarfs, we adopt the mass-luminosity relation given by Henry & McCarthy (1993) for CMR (1) and an interpolation between relations based on different metallicities (Baraffe et al. 1998) for CMR (2) (see §3.3 for details).

The statistical uncertainties are reduced considerably when all the available data are taken into account. The new results are basically consistent with the previous ones. Stars in the sample are detected as far as on the "top" of the disk. See Figure 2. The average height for the weighted distribution is about 2 kpc for the solar-neighborhood CMR (1). Therefore, the scale length H we measure is in fact that of the kinematically hottest and hence most metal-poor component of the disk, which is often called the "old" or "thick" disk. Optical studies prior to 1990 support a disk scale length of 3.5–4.5 kpc (see Sackett 1997 and references therein). More recent studies, on the contrary, tend to give a shorter scale length. Paper I and Paper II give estimates of the scale length to better precision than other methods. Our results here also favor a short scale length, 3.3 kpc. This is the most precise measurement of the scale length of the old or thick disk up to now with a statistical uncertainty less than 6%. At this stage, the systematic errors become significant with respect to the statistical errors which motivates our modification of the CMR. If the z-dependent CMR (2) is adopted, stars tend to be fainter and therefore closer at a given color, and the disk scale length is therefore smaller, i.e. 2.75 kpc. We estimate the systematic error to be half of the difference between the best-fit results using the solar-neighborhood CMR (1) and z-dependent CMR (2), respectively. We finally express the disk scale length to be $H = 2.75 \pm 0.16$ (statistical) ± 0.25 (systematic) kpc. Our measurement is based on low mass stars which dominate the stellar mass in the disk so that the scale length we derive is likely to reflect the stellar mass distribution in the disk.

3.3. Mass Function

To convert the LF to the mass function (MF) for the solar-neighborhood CMR (1), we use the empirical mass- M_V relation given by Henry & McCarthy (1993) (see their eq. [5]). The mass function Φ_M is defined as the number density of stars N per decade in mass and it usually can be characterized by a power law:

$$\lg \Phi_M = \lg(dN/d\lg M) = \lg(M^{-\alpha}) + \alpha : \quad (7)$$

Similar to the results of Papers I & II, the MF in the range of $0.08M_\odot < M < 0.6M_\odot$ obtained in this

Table 3. Best-Fit Models for M Stars ($8 < M_V < 18.5$)(Only best-fit sech^2 models are listed here for Paper I and Paper II.)

Data Set	h ₁ (pc)		h ₂ (pc)		(%)		ρ ₀ (M pc ⁻³)		M (M pc ⁻²)		H (kpc)	
Paper I	323	54	656	78	19.8	7.1	0.0159	0.0044	12.4	1.9	3.02	0.43
Paper II	320	50	643	60	21.6	6.8	0.0158	0.0041	12.3	1.8	2.92	0.40
Paper II (corrected)	314	52	627	55	23.7	7.3	0.0161	0.0043	12.5	1.8	2.95	0.41
All but PC Data, CM R (1)												
sech ² M odel	327	32	604	28	21.9	4.2	0.0207	0.0040	16.1	1.9	3.28	
exp M odel	185	21	609	30	10.1	2.3	0.0437	0.0106	19.9	2.7	3.28	
norm alized	-		-		-		0.0183		15.7	2.1	3.28	
All but PC Data, CM R (2)												
sech ² M odel	264	60	435	18	53.6	13.0	0.0191	0.0049	13.6	1.8	2.75	
exp M odel	149	40	434	19	33.2	13.2	0.0309	0.0125	15.1	2.6	2.75	
norm alized	-		-		-		0.0156		13.1	2.5	2.75	
All Data, CM R (1)												
sech ² M odel	332	31	609	28	24.4	4.2	0.0179	0.0030	14.3	1.4	3.28	0.18
exp M odel	193	22	614	31	12.1	2.5	0.0347	0.0071	16.9	1.8	3.28	0.18
norm alized	-		-		-		0.0180		14.3	1.3	3.28	0.18
All Data, CM R (2)												
sech ² M odel	270	55	440	18	56.5	11.5	0.0169	0.0034	12.4	1.3	2.75	0.16
exp M odel	156	40	439	19	38.1	12.6	0.0253	0.0081	13.4	1.8	2.75	0.16
norm alized	-		-		-		0.0153		12.2	1.6	2.75	0.16

Table 4. Normalized Mass Functions

(Both MFs are derived using all the available data. Here ρ_M is defined as $dN(\text{number}=\text{pc}^3)=d \lg M$.)

CM R (1)	$\lg \rho_M$		CM R (2)	$\lg \rho_M$	
$\lg(M-M_\odot)$			$\lg(M-M_\odot)$		
-0.20	-1.21	0.08	-0.24	-1.25	0.13
-0.24	-1.06	0.05	-0.29	-1.32	0.08
-0.29	-1.02	0.04	-0.39	-1.24	0.05
-0.43	-1.15	0.03	-0.52	-1.10	0.04
-0.60	-1.12	0.03	-0.67	-0.97	0.04
-0.76	-1.29	0.04	-0.80	-1.13	0.05
-0.85	-1.25	0.05	-0.90	-1.15	0.06
-0.97	-1.53	0.06	-0.98	-1.26	0.08
-1.09	-1.33	0.08	-1.06	-1.27	0.10

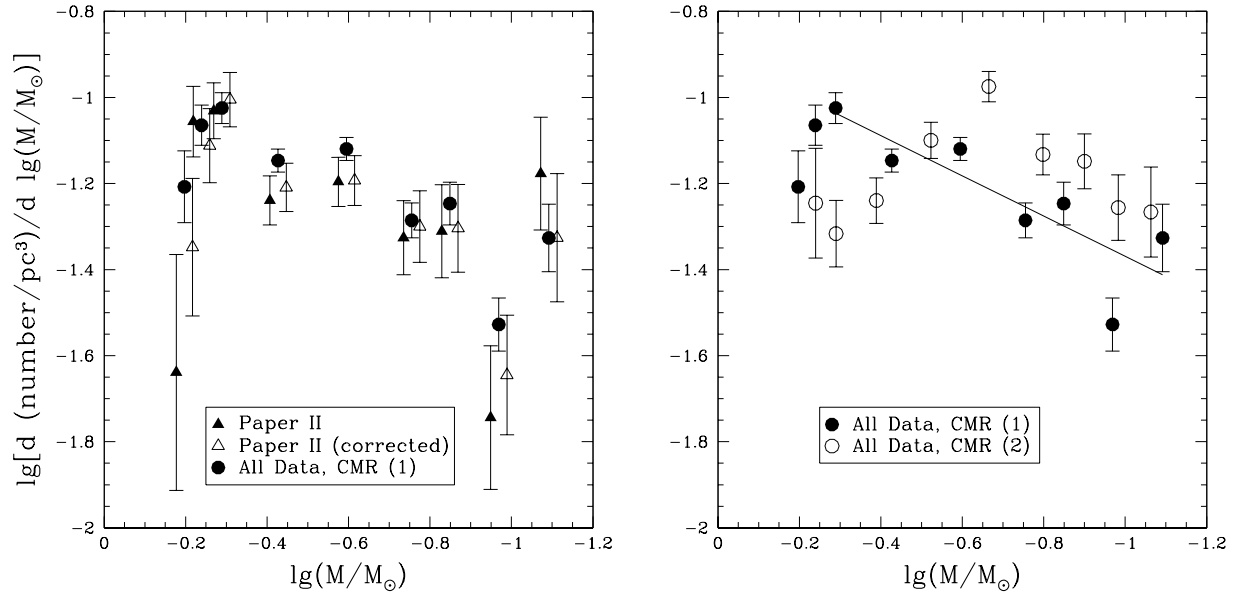


Fig. 4. | Mass functions from LFs. The symbols and labels have the same meanings as those in Fig. 3. In the left panel, the three MFs are slightly displaced along the horizontal direction with respect to each other. In the right panel, we also show the best power law fit to the MF in the case of using the solar-neighborhood CMR (1): $\lg M = 0.90 + 0.47 \lg(M/M_\odot)$ (the first two data points are excluded from the fit), where $M = dN/d \lg M$ and N is the number density of stars.

paper tends to fall towards the lower mass (see Fig. 4). The statistical errors are now reduced considerably, especially for the first and the last two bins.

There are two structures in the MF derived from CM R (1). First, there appears to be a break in the slope of the MF at about $0.5M_{\odot}$. The MF tends to rise from $0.6M_{\odot}$ ($\lg(M/M_{\odot}) = 0.2$) to $0.5M_{\odot}$ ($\lg(M/M_{\odot}) = 0.3$) and after that it drops toward the lower mass. Whether there is a break in the MF still is a matter of debate. The MF from the LF of Wielen et al. (1983) shows such a break. The results of Papers I and II, combined with the Wielen et al. (1983) MF at higher masses, reinforce the case for a break (see Fig. 3 of Paper II). Taking Hipparcos data into account changes somewhat the Wielen et al. (1983) LF. See the 25 pc limited sample of Jahreiss & Wielen (1997). These changes cause the first four points in Figure 3 of Paper II to increase somewhat, but the break in the slope is still pronounced. However, Reid & Gizis (1997) analyzed an 8-pc sample and found no evidence for a break point in the MF. Instead the MF rises gradually toward the lower mass (see their Fig. 4). The hint of a break point in the MF we derived for CM R (1) is at the level of 2σ , so it is very marginal. The second structure in the MF is the dip at $0.1M_{\odot}$. This dip is detected at the 3σ level and so is of high statistical significance. However, it is possible that this dip is an artifact of subtleties in the structure of the CM R or mass-luminosity relation that are not reflected in our simple model.

For the solar-neighborhood CM R (1), the power law fit to the MF agrees very well with the result in Paper II. After correcting the error estimation and applying the new photometry transformation for data used in Paper II, we get a power law fit of the MF with a slope $= 0.43 \pm 0.11$ and a zeropoint $= 0.97$. When all the available data are taken into account, the slope becomes $= 0.41 \pm 0.06$ and $= 0.94$. If we do the fit only using the data points after the possible break point, $M = 0.5M_{\odot}$, we get $= 0.47 \pm 0.07$ and $= 0.90$.

For CM R (2), we modify the CM R to reflect the metallicity gradient above the Galactic plane. Therefore, to derive the MF in this case, the metallicity effect on the mass- M_V relation must also be taken into account. Less luminous stars are most likely to be nearby stars (see Fig. 1) and are therefore little affected by the metallicity gradient. We assume that, from the plane to a height $z = 1500$ pc, the metallicity changes linearly from $[M/H] = 0.0$ to $[M/H] = 0.5$ and keeps the value 0.5 above $z = 1500$ pc. We calculate the mean height above the Galactic plane of the stars in our sample in each magnitude bin. We then obtain a linearly interpolated mass- M_V relation at these mean heights, respectively, using mass- M_V relations for $[M/H] = 0.0$ and $[M/H] = 0.5$ given by Baraffe et al. 1998. The $[M/H] = 0.0$ mass- M_V relation by Baraffe et al. 1998 agrees with that by Henry & McCarthy (1993). The resultant MF is shown in Fig. 4. This MF has a dip at $0.5M_{\odot}$ and a peak at $0.2M_{\odot}$. However, these features may be caused by the somewhat ad hoc CM R and the averaged mass- M_V relation that we adopt. Thus, the detailed structure in the MF should not be given much credence. More reliable is the overall slope $= 0.10$. In Paper II, we advocated a correction to the slope due to unresolved binaries of $+0.35$. Our final slope corrected for binaries is therefore

$$0.45 \quad [\text{CM R (2); corrected for binaries}]; \quad (8)$$

MFs derived using all the available data and adopting different CM Rs are tabulated in Table 4.

3.4. Mass Density and Microlensing

As we described in §3.1, the LF we finally get is the linear combination of LFs from the sech^2 model and the double exponential model that satisfies the local normalization (Wielen et al. 1983) in

the range $8.5 < M_V < 12.5$. The normalized local mass densities for the solar-neighborhood CMR (1) is $\rho_0 = 0.0180 M_\odot \text{ pc}^{-3}$ which is about 12% higher than those in Paper I and II but is consistent at the 1 σ level. The normalized local mass densities for the z-dependent CMR (2) is $\rho_0 = 0.0153 M_\odot \text{ pc}^{-3}$.

The normalized local surface density for CMR (1) is $\Sigma_M = 14.3 M_\odot \text{ pc}^{-2}$, which is 15% higher than those in Papers I & II, while the normalized local surface density for CMR (2) is $\Sigma_M = 12.2 M_\odot \text{ pc}^{-2}$. Our estimate of the total column density of the disk (gas plus stars, see Paper I) does not change much ($\Sigma_{\text{obs}} = 43 M_\odot \text{ pc}^{-2}$ for CMR (1) and $\Sigma_{\text{obs}} = 41 M_\odot \text{ pc}^{-2}$ for CMR (2)).

How much do the stellar contents contribute to the optical depth of microlensing towards the Large Magellanic Cloud (LMC)? For the exponential component of a disk, the optical depth $\tau = 2 G h \csc^2 b = c^2$, and for the sech^2 component, the optical depth $\tau = 2 (\ln 2) G h \csc^2 b = c^2$ where $b = 33^\circ$ is the Galactic latitude of the LMC and Σ is the local surface density of stars. The estimate of the optical depth from our data is about 1.2×10^{-8} for either CMR (1) or CMR (2). Thus the disk stars contribute only 8% of the optical depth 1.2×10^{-7} determined by the MACHO collaboration (Alcock et al. 2000a). If we assume the disk profile we report here extends all the way to the Galactic center, we can also estimate the contribution of disk stars to the optical depth of microlensing towards sources in Baade's Window ($(l, b) = (1^\circ; 4^\circ)$). We further assume that other stars are distributed like M dwarfs and the density ratio of other stars to M dwarfs is constant. Under these conditions, the optical depth is estimated to be 4.1×10^{-7} for CMR (1) or 5.2×10^{-7} for CMR (2) which is only about 20% of the value measured by the MACHO collaboration (Alcock et al. 2000b). These numbers are very close to the original estimates of Paczynski (1991) and Griest et al. (1991). Subsequently, Kiraga & Paczynski (1994) realized that the optical depth toward Baade's Window is dominated by bulge stars, not disk stars. However, this close agreement is something of a coincidence. In this paper we derive both a lower local stellar density and a shorter disk scale length than was adopted by these authors. Each of these leads to a change by a factor ~ 1.4 in the optical depth, but in opposite directions. We caution that our calculation of the optical depth towards Baade's Window is mainly for illustrative purpose since extending the disk profile to the Galactic center involves a substantial extrapolation from the data. By contrast, we expect that our optical depth estimate towards the LMC is reasonably accurate.

4. CONCLUSIONS

In this paper, we study M dwarfs from Hubble Space Telescope star counts. The sample is about four times larger than that studied in Paper II. This large sample considerably reduces the statistical errors which leads to the most precise determination of the M dwarf disk profiles to date. We also investigate the effects of systematic errors by using a modified color-magnitude relation which depends on Galactic height. The basic results are consistent with those in Paper I and II: the LF peaks at about $M_V = 12$ and has a sharp drop toward $M_V = 14$. The MF $dN/d \lg M / M$ has a power-law index $\alpha = 0.47 \pm 0.07$ for the solar-neighborhood CMR (1) and $\alpha = 0.10$ for the z-dependent CMR (2), both before the correction for binaries. Our analysis favors a short scale length, $H = 2.75 \pm 0.16$ (statistical) ± 0.25 (systematic) kpc, for the M dwarf disk population lying ~ 2 kpc above the plane.

Work by Z.Z., A.G., and S.S. was supported in part by grant AST 97-27520 from the NSF. A.G. received additional support from Le Ministere de L'Education Nationale de la Recherche et de la Technologie.

APPENDIX : GROUND-BASED CALIBRATION OF HST W FPC2 PHOTOMETRY OF RED STARS

For many astrophysical purposes, the use of standard Johnson-Cousins photometric system is necessary, as most of the ground-based results are expressed in this system. The Hubble Space Telescope (HST) Wide Field and Planetary Camera 2 (WFPC2) has its own set of filters with transmission profiles different from those of Johnson-Cousins system. A calibration between the two systems is required – in this case between WFPC2 F606W and F814W filters and standard V and I filters, to which they roughly correspond. And in this particular case, the calibration has to be valid for the very red stars.

The most widely used such calibration is that by Holtzman et al. (1995, hereafter H95). They give a synthetic calibration for F606W based on convolutions of WFPC2 response curves with stellar spectra from the Bruzual, Persson, Gunn & Stryker atlas (available from STScI ftp site.) While H95 do give an empirical calibration for F814W, it is derived using the ground-based observations of stars that were "not very red". The authors suggest that for red stars one should switch from the empirical transformations to the synthetic ones.

Bahcall et al. (1994, hereafter BFGK) give another synthetic calibration. They transformed F606W and F814W magnitudes into V and I using theoretical throughput and response curves and convolving them with Gunn & Stryker (1983) standard spectra. A comparison between H95 and BFGK transformations indicates some differences both in zero points and in color terms. There is an obvious need for an empirical ground-based calibration, which one would want in any case. Any such calibration should include red stars ($V - I > 3$).

It should be noted that transformations as given by H95 apply to WFPC2 CCDs after the 1994 Apr 23 cooldown from 76°C to 88°C, while BFGK transformations apply to observations made before the cooldown. The cooldown reduced the CTE (Charge Transfer Efficiency) effect and increased the QE (Quantum Efficiency).

We have performed a ground-based calibration based on stars observed in a portion of the Groth Strip, 28 contiguous WFPC2 fields. Our single CCD field spans approximately 9 original WFPC2 fields (~ 36 arcmin²). We chose the Groth Strip because, in contrast to most WFPC2 fields, the size of the field is well-matched to ground-based CCDs and because photometry of its stellar contents was already available (Paper II). We selected the field so as to include as many red ($V - I > 3$) stars as possible.

The observations were performed on the Hiltner 2.4-m telescope at the MDM Observatory, using the Echelle CCD camera with SITE 2048 \times 2048 detector. We obtained a total of 7200 s in V and 6000 s in I, in photometric conditions and 1'' seeing. Photometry was performed to limiting magnitudes of $V = 25.1$ and $I = 23.6$. Photometry was reduced using observations of Landolt (1992) standards (as red as $V - I = 4.00$ for V and $V - I = 3.48$ for I), and standard procedures in IRAF. Color terms needed to transform instrumental into standard magnitudes are: -0.004 ± 0.005 for V, and -0.031 ± 0.007 for I.

WFPC2 images of the Groth Strip for which we have photometry were taken before the 1994 Apr 23 cooldown, during the time when the effects of CTE were more pronounced. The only reason that we use pre-cooldown observations, although the vast majority of observations were made after the cooldown, is that these observations are unique in terms of sky coverage. Deep fields observed after the cooldown are mostly single fields, therefore containing few of the red stars that are needed for the calibration. In order to correct for CTE, we used the CTE model with coefficients for 76°C, given by Stetson (1998). Our WFPC2 images have a background of 50 e⁻/pixel in F606W (exposure time 700 s) and 44 e⁻/pixel

in F814W (exposure time 1100 s). We used these background levels to evaluate CTE corrections for each individual star. Corrections turned out to be between 0.01 and 0.07 mag. According to Stetson (1998), these CTE corrections include position independent charge loss and should eliminate the apparent problem of "long vs. short" exposures.

Out of approximately 75 stars in our field that were measured on the WFPC2 in ages (8 of them red), we were able to detect some 50. This number was reduced to 34 stars in V (4 of them red) and 40 stars in I (all 8 red stars detected) after excluding stars that were contaminated by close-lying galaxies in the ground-based photometry (as cross-checked with HST in ages) and those that were saturated in the HST photometry.

BFGK introduce chip-to-chip zero-point offsets that are to be applied to each of the chips 2, 3 and 4 of WFPC2 (designated as n , $n = 2;3;4$), because of different response curves of chips. We checked the validity of these offsets by measuring the mean differences between the BFGK HST V and I magnitudes and our ground-based magnitudes separately for each chip. Our results show that these offsets are not needed. The likely reason for this is that the chip sensitivity differences are accounted for by the offsetting that is normalized to the WF3 chip only. Any remaining chip-to-chip offsets must be very small.

Now we present our best fits to the residuals between our ground-based data and the magnitudes from the H95 and BFGK transformations. To obtain the fits, we weighted the data points by the photometric errors scaled up to produce reduced $\chi^2 = 1$. The zero points and errors were obtained from fits centered at $V - I = 2$, in order to reduce correlation between the zero point and slope (color-term) errors.

Since our WFPC2 observations were made prior to the cooling, the zero points will not be the same if one uses observations at the lower temperature. In that case one should add $V_{CD} = 0.044$ and $I_{CD} = 0.007$ (Whitmore 1995). Otherwise, for pre-cooling observations, $V_{CD} = I_{CD} = 0$.

The corrections to the H95 calibration are,

$$V = V_H + \Delta V_H; \quad \Delta V_H = [0.058(0.010) + V_{CD}] - 0.037(0.013)(V - I - 2); \quad (1)$$

$$I = I_H + \Delta I_H; \quad \Delta I_H = [0.004(0.012) + I_{CD}] + 0.004(0.012)(V - I - 2); \quad (2)$$

where V_H and I_H are the transformations given by equation (9) in H95, with zero points and first and second order color-terms given in Table 10 of H95.

Since H95 was derived with post-cooling observations, $V_{CD} = 0.044$ and $I_{CD} = 0.007$. The correction in I is not significant. At our adopted midpoint, $V - I = 2$, our V-band calibration is in good agreement with H95, $\Delta V_H = 0.014 \pm 0.010$. However, we find a difference in slope of 0.037, which means that the redder stars are slightly bluer.

The corrections to the BFGK calibration are,

$$V = V_B + \Delta V_B; \quad \Delta V_B = [0.059(0.011) + V_{CD}] - 0.040(0.014)(V - I - 2); \quad (3)$$

$$I = I_B + \Delta I_B; \quad \Delta I_B = [0.007(0.014) + I_{CD}] + 0.022(0.013)(V - I - 2); \quad (4)$$

where V_B and I_B are the transformations given by equation (2.1) in BFGK, but with $n = 0$, as previously explained. The BFGK zero points and color-terms are given in the text of BFGK, below their equation (2.1).

Again, the corrections to I_B are small. For V_B , we find the same slope offset, but the zero-point offset is much larger than for V_H .

REFERENCES

- Alcock, C., et al. 2000a, ApJ submitted (astro-ph/0001272)
- Alcock, C., et al. 2000b, ApJ submitted (astro-ph/0002510)
- Bahcall, J.N. 1986, ARAA, 24, 577
- Bahcall, J.N., Flynn, C., Gould, A., & Kirhakos, S. 1994, ApJ, 435, L51 (BFGK)
- Bahcall, J.N., Maoz, D., Doxsey, R., Schneider, D.P., Bahcall, N.A., Lahav, O., & Yanny, B. 1992, ApJ, 387, 56
- Baran, I., Chabrier, G., Allard, F., & Hauschildt, P.H. 1998, A & A, 337, 403
- Burstein, D., & Heiles, C. 1982, AJ, 90, 817
- Gizis, J.E. 1997, AJ, 113, 806
- Gould, A. 1995, ApJ, 440, 510
- Gould, A., Bahcall, J.N., & Flynn, C. 1996, ApJ, 465, 759 (Paper I)
- Gould, A., Bahcall, J.N., & Flynn, C. 1997, ApJ, 482, 913 (Paper II)
- Gould, A., Bahcall, J.N., & Maoz, D. 1993, ApJS, 88, 53
- Green, E.M., Demarque, P., & King, C.R. 1987, The Revised Yale Isochrones and Luminosity Functions (New Haven: Yale Univ. Obs.)
- Griest, K., et al. 1991, ApJ, 372, L79
- Gunn, J.E. & Stryker, L.L. 1983, ApJS, 52, 121
- Hawkins, M.R.S., & Bessel, M.S. 1988, MNRAS, 234, 177
- Henry, T.J., & McCarthy, D.W. 1993, AJ, 106, 773
- Holtzman, J.A. et al. 1995, PASP, 107, 1065 (H95)
- Jahreiss, H., & Wielen, R. 1997, HIPPARCOS '97. Presentation of the Hipparcos and Tycho catalogues and first astrophysical results of the Hipparcos space astrometry mission, ed. B. Battistini, M.A.C. Perryman, & P.L. Benvenuti, 675
- Kiraga, M., & Paczynski, B. 1994, ApJ, 430, L101
- Kirkpatrick, J.D., McGraw, J.T., Hess, T.R., Liebert, J., & McCarthy, D.W., Jr. 1994, ApJS, 94, 749
- Landolt, A.U. 1992, AJ, 104, 340
- Maoz, D., et al. 1993, ApJ, 409, 28
- Monet, D.G., Dahn, C.C., Vrba, F.J., Harris, H.C., Pier, J.R., Luginbuhl, C.B., & Ables, H.D. 1992, AJ, 103, 638
- Paczynski, B. 1991, ApJ, 371, L63
- Reid, I.N. 1991, AJ, 102, 1428
- Reid, I.N., & Gizis, J.E. 1997, AJ, 113, 2246
- Sackett, P.D. 1997, ApJ, 483, 103
- Stetson, P.B. 1998, PASP, 110, 1448
- Tinney, C.G., Reid, I.N., & Gould, J.R. 1993, ApJ, 414, 254
- Whitmore, B. 1995, (Calibrating HST: Post Servicing Mission)

W ielen, R ., Jahreiss, H ., & K ruger, R . 1983, IAU Colloq. 76, Nearby Stars and the Stellar Lum inosity Function, ed. A G D .Philip & A R .Upgren (Schenectady: L.D avis), 163